Chemical Science

ROYAL SOCIETY OF CHEMISTRY

EDGE ARTICLE

View Article Online
View Journal

Cite this: DOI: 10.1039/d6sc00807k

All publication charges for this article have been paid for by the Royal Society of Chemistry

Chemical regulation of carbonization enables structure-tailored hard carbon anodes from recycled polypropylene separators

Mingyue Wang,* Yue Wang, Na Li, Qing Zhong, Min Zhu, Dongyang Zhang and Shujiang Ding *

The efficient recycling of spent lithium-ion battery separators and the rational design of hard carbon anodes are critical for the development of sustainable sodium-ion batteries. Herein, a sulfonation-induced crosslinking strategy is proposed to regulate the carbonization behavior of recycled polypropylene (PP) separators, enabling their direct conversion into structure-tailored hard carbon *via* a one-step carbonization process. Sulfonation not only introduces sulfonic functionalities but, more importantly, induces intermolecular crosslinking, which suppresses severe chain scission and volatilization during thermal treatment and transforms the decomposition pathway into a solid-state carbonization process. As a result, the structure-tailored HC is constructed by chemically regulating the carbonization behavior of recycled PP separators, enabling efficient sodium storage with clarified structure–sodium storage correlation. When applied as an anode for SIBs, the PP-derived HC exhibits a high reversible capacity of 293.0 mAh g^{-1} at 0.2C and superior rate capability of 77.1 mAh g^{-1} at 10C. For long-term cyclic performance, the capacity remained at 222.7 mAh g^{-1} after 1000 cycles at 1C with a capacity retention of 89.1%. When coupled with an $Na_3V_2(PO_4)_3$ cathode, the full cell can deliver a capacity of 83.0 mAh g^{-1} after 200 cycles with 80.1% retention. This work demonstrates that chemical regulation of the carbonization pathway provides an effective route for both high-value separator recycling and structure-oriented hard carbon design for sodium-ion batteries.

Received 29th January 2026
Accepted 5th March 2026

DOI: 10.1039/d6sc00807k

rsc.li/chemical-science

1. Introduction

With the increasing penetration of renewable energy sources and the growing demand for large-scale energy storage systems, the development of low-cost, resource-abundant, and safe rechargeable batteries has attracted considerable attention.[1–3] Sodium-ion batteries (SIBs) have emerged as promising alternatives to lithium-ion batteries (LIBs) owing to their similar working principles and high compatibility with existing battery manufacturing lines. More importantly, SIBs offer several intrinsic advantages, including significantly lower costs (approximately 30–40%), high security, and superior low-temperature performance, which make SIBs particularly attractive for next-generation grid-scale energy storage applications.[4,5] However, the larger ionic radius and sluggish diffusion kinetics of Na^+ ions pose significant challenges for electrode materials, particularly for the anode, which remains a key bottleneck for the practical application of SIBs.

Among various anode candidates, hard carbon (HC) has been widely recognized as the most viable option for SIBs due to its low operating potential, relatively high reversible capacity, and excellent cycling stability.[6,7] Nevertheless, the sodium storage behavior of HC is highly dependent on its microstructural features, including the degree of disorder, the interlayer distance of the graphitic layers, and the distribution of pores.[8,9] It is generally accepted that the sloping region in the voltage profile is associated with sodium adsorption at defect sites and surface regions, whereas the low-potential plateau capacity is closely related to sodium insertion between graphene layers or filling of nanopores.[10,11] Despite extensive studies, a clear correlation between structural parameters and sodium storage behavior has not yet been fully established, which hinders the rational design of HC anodes with optimized performance.

In terms of HC precursors, biomass, coal, and petroleum pitch have been extensively explored for the large-scale production of HC and have demonstrated promising electrochemical performance in SIBs.[12–14] However, these precursors often possess complex and heterogeneous chemical compositions, and their carbonization behavior is strongly dependent on the intrinsic characteristics of the raw materials. As a result, achieving accurate structural control and batch-to-batch consistency remains challenging. In contrast, polymer-based

School of Chemistry, Engineering Research Center of Energy Storage Materials and Devices, Ministry of Education, National Innovation Platform (Center) for Industry-Education Integration of Energy Storage Technology, Xi'an Jiaotong University, Xi'an 710049, P. R. China. E-mail: mywang@xjtu.edu.cn; dingsj@xjtu.edu.cn

precursors offer advantages, such as well-defined chemical composition and tunable molecular structures, providing opportunities to regulate the carbonization pathway and tailor the resulting HC structure.[15,16] Nevertheless, typical polyolefin polymers, such as polypropylene (PP, with ~33 at% carbon content), undergo severe chain scission and rapid volatilization during thermal decomposition, leading to extremely low carbon yields and poorly developed carbon frameworks, which largely limit their direct use for HC anodes.[17]

Notably, PP separators are extensively used in commercial lithium-ion batteries and generate a large amount of waste at the end of battery life. At present, spent separators are mainly treated by incineration or low-value recycling, resulting in both resource waste and environmental concerns. In this regard, waste PP separators exhibit high purity, uniform composition, and a centralized source, making them attractive candidates as carbon precursors.[18–20] However, overcoming the intrinsic thermal instability of PP during carbonization and transforming waste separators into structurally suitable HC materials remain critical scientific and technological challenges.

In this work, we propose a chemical sulfonation-induced crosslinking strategy to regulate the carbonization behavior of recycled PP separators, as shown in Fig. 1. By introducing crosslinked networks between polymer chains, the thermal decomposition pathway of PP is effectively modified, suppressing excessive volatilization and enabling the formation of stable carbon frameworks during a one-step carbonization process. The resulting HC materials exhibit tunable microstructures, including controlled disorder, interlayer spacing, and pore characteristics. Furthermore, by employing these materials as anodes for SIBs, we systematically investigate the relationship between structural features and sodium storage behavior. This study not only provides a feasible approach for the high-value recycling of spent LIB separators but also offers insights into the structure–sodium storage correlation in HC, contributing to the rational design of advanced HC anodes for SIBs.

2. Results and discussion

Recycled PP separators consist of linear polyolefin chains with saturated –C–C– backbones and pendant $–CH_3$ groups. Owing to the absence of aromatic units or thermally stable functional groups, recycled PP typically undergoes rapid β-scission and extensive volatilization upon heating, leading to negligible carbon yield and the failure to form a continuous carbon framework.[21,22] As shown in the DSC results in Fig. 2a, the endothermic peaks at 140–170 °C correspond to the melting of the PP separator, while the peaks at 420–480 °C are assigned to the decomposition of the PP separator. This intrinsic thermal instability fundamentally limits the direct conversion of PP into hard carbon. Interestingly, the PP separator after sulfonation can be transformed into carbon with 50.9% yield, as presented in Fig. 2b, which reveals an elevated decomposition onset temperature and a significantly increased char yield for sulfonated PP compared with recycled PP, indicating a transition from a volatilization-dominated decomposition pathway to a solid-state carbonization process. This phenomenon is attributed mainly to the sulfonic functionalities ($–SO_3H$) introduced onto the PP chains *via* sulfonation treatment. Due to lower bond dissociation energy, higher carbocation stability during electrophilic substitution, and reduced steric hindrance along the PP backbone of tertiary C–H bonds, sulfonation is expected to occur preferentially at the more reactive tertiary C–H sites along the PP backbone, while substitution at the methyl side chains is much less favorable. Beyond simple functionalization, sulfonation induces the formation of a crosslinked polymer network, which plays a decisive role in regulating the subsequent thermal decomposition behavior. The crosslinked structure effectively restricts polymer chain mobility, suppresses melt-flow, and inhibits severe depolymerization during heating.[23,24]

To further reveal the sulfonation effect on the PP separator, the structure and functional groups of the sulfonated PP

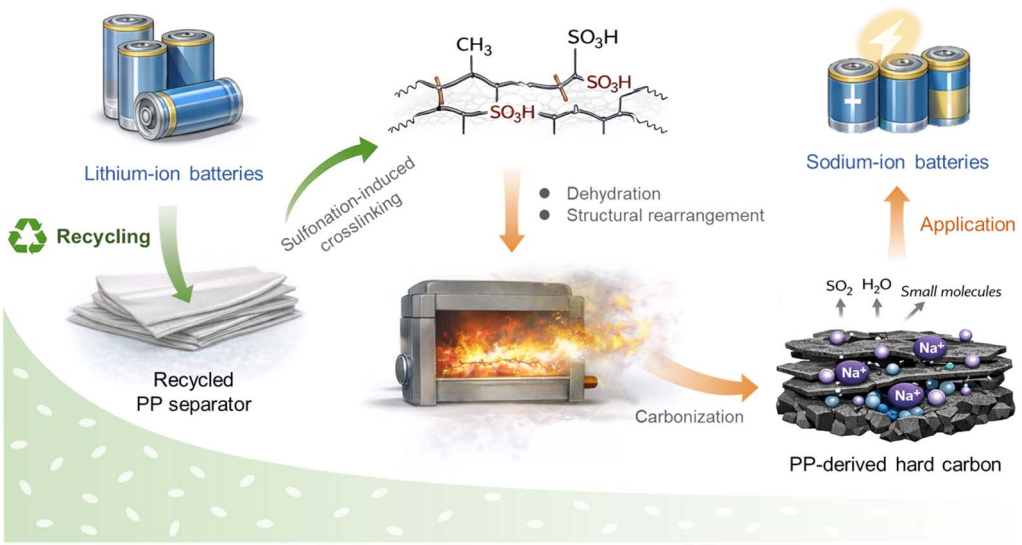

Fig. 1 Schematic diagram of the synthesis of recycled PP-derived hard carbon.

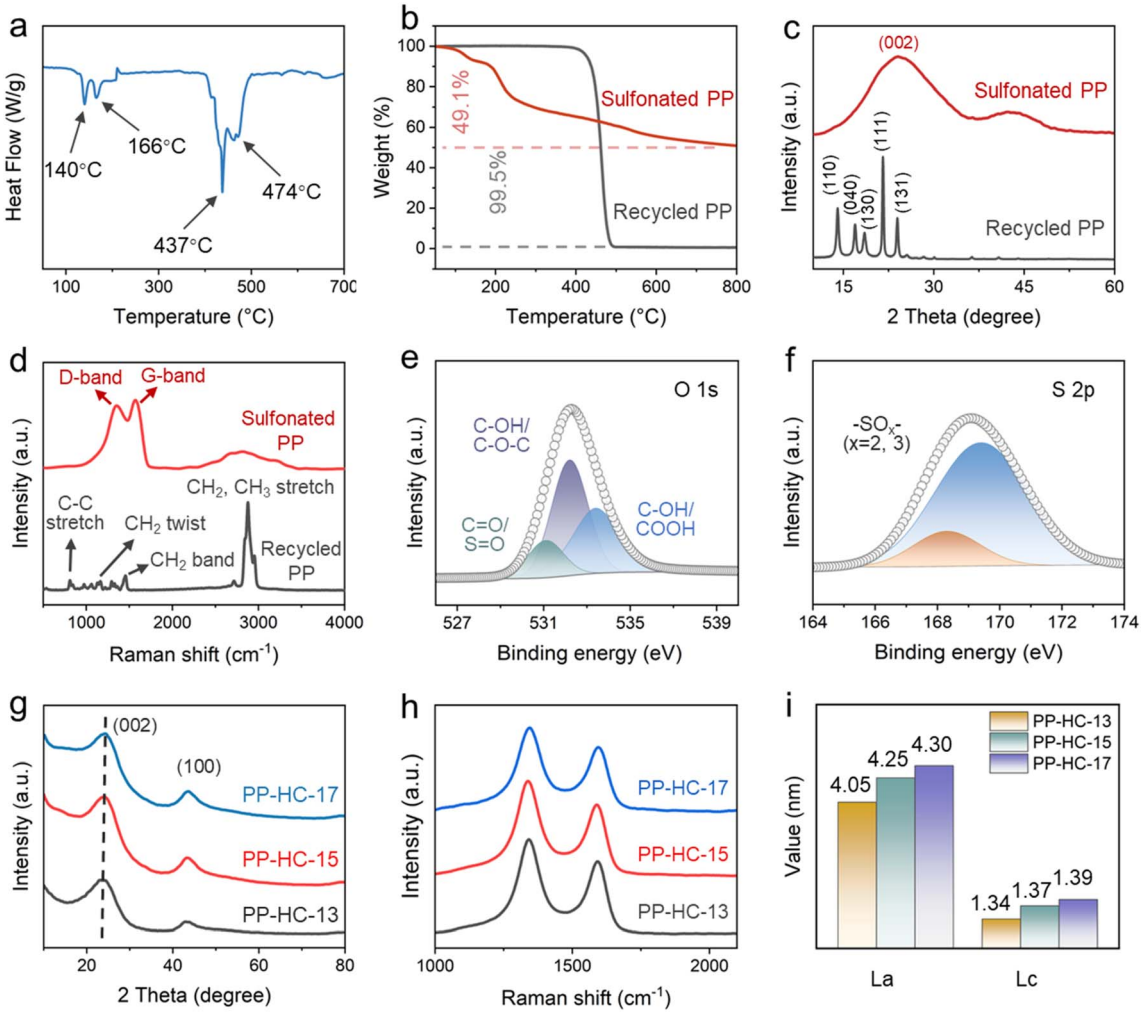

Fig. 2 (a) DSC curve of recycled PP separator. (b) TG curves, (c) XRD patterns, and (d) Raman curves of recycled PP separator and sulfonated PP separator. High-resolution XPS spectra of (e) O 1s and (f) S 2p in sulfonated PP separator. (g) XRD patterns, (h) Raman curves, and (i) L_a and L_c values of PP-HC-13, PP-HC-15, and PP-HC-17 samples.

separator were analyzed. XRD reveals the crystal structure of PP and sulfonated PP separators, as provided in Fig. 2c. The XRD pattern of a recycled PP separator showed sharp peaks corresponding to the typical monoclinic PP structure.[25] After sulfonation, all these diffraction peaks consisted of two broad peaks, demonstrating the destruction of the crystal structure of the PP separator during sulfonation treatment. Additionally, the peaks below 1500 cm^{-1} and between 2700 and 3000 cm^{-1} in the Raman spectra of the recycled PP separator (Fig. 2d) originate from C–C stretching and $–CH_2$, $–CH_3$ asymmetric and symmetric stretching. However, the Raman spectrum of the sulfonated PP separator shows two distinct peaks corresponding to the defect-induced band (D-band) and the crystalline graphite band (G-band), along with a broad band at 2500–2800 cm^{-1}, consistent with the spectrum of amorphous carbon, demonstrating the formation of aromatic rings. Furthermore, the O 1s XPS spectrum of a sulfonated PP separator shown in Fig. 2e can be divided into three peaks, corresponding to phenols (C–OH(ph))/COOH, epoxide groups (C–OH/C–O–C), and C═O/S═O. While the S 2p spectrum in Fig. 2f reveals the existence of $–SO_x–$ bonds, indicating the generation of sulfonyl groups.

During carbonization, the sulfonated and crosslinked PP precursor undergoes a series of dehydration, dehydrogenation, and structural condensation reactions at intermediate temperatures. In this stage, sulfur-containing groups are progressively decomposed, releasing SO_2, H_2O, and other small molecules. Although most sulfur species are removed at elevated temperatures, they serve as structure-directing agents in the early stage of carbonization by promoting intermolecular crosslinking and stabilizing the evolving carbon skeleton. This behavior prevents the premature collapse of the framework and enables continuous structural rearrangement toward a carbonaceous network. With a further increase in temperature, the constrained carbon skeleton undergoes aromatization and develops short-range ordered, turbostratic carbon domains composed of randomly stacked graphene-like layers. The presence of crosslinking limits long-range layer rearrangement and suppresses

graphitization. The carbon yield of the HC is around 48%. As shown in Fig. 2g, the XRD patterns of the samples carbonized at 1300, 1500 and 1700 °C exhibit two broad peaks at 20–30° and 40–50°, which can be indexed to the (002) and (100) planes of disordered carbon, respectively. Additionally, the interlayer distances of PP-HC-13, PP-HC-15 and PP-HC-17 are calculated to be 0.374, 0.371, and 0.367 nm, respectively. The Raman spectra shown in Fig. 2h exhibit the characteristic peaks of the D-band at around 1350 cm^{-1} and the G-band at around 1580 cm^{-1}, demonstrating the amorphous nature of the structure.[26] As calculated, the intensity ratios of the G-band to the D-band (I_G/I_D) of HC-13, PP-HC-15 and PP-HC-17 are 0.749, 0.765 and 0.772, indicating the increased graphitization of PP-HC along with the increasing carbonization temperature. Accordingly, the lateral width (L_a) and stacking height (L_c) are also enhanced with the elevated temperature, as presented in Fig. 2i.

To analyze the morphology and microstructure of the as-prepared PP-HC, scanning electron microscopy (SEM) and transmission electron microscopy (TEM) testing were carried out. First, the turbostratic carbon domains can be observed in the high-resolution TEM (HRTEM) images in Fig. 3a–c, in which the interlayer distance can be measured as 0.367, 0.371 and 0.374 nm for PP-HC-13, PP-HC-15 and PP-HC-17 samples, respectively, in line with the results of XRD analysis. Fig. 3d provides SEM images of the PP-HC samples, which possesses a uniform micro-scale block structure and contains a small amount of S element. The C 1s XPS spectra of the three HC samples in Fig. 3e demonstrate that the four deconvoluted peaks are assigned to sp^2-C, sp^3-C, S–O/C–S and C=O.[27,28] As can be observed, the contents of sp^2-C are increased (Fig. 3f) and oxygen-containing functional groups are decreased with the elevation in carbonization temperature. Meanwhile, gas evolution associated with functional group decomposition and incomplete shrinkage of the crosslinked framework during carbonization of the sulfonated PP separator generates defects and nanopores. Then, the pore structures of the as-prepared samples were evaluated by N_2 adsorption–desorption testing. As a result, the specific surface areas (SSAs) of PP-HC-13, PP-HC-15 and PP-HC-17 are 99.4, 85.4 and 74.8 $m^2\ g^{-1}$, respectively, while the pore volumes of PP-HC-13, PP-HC-15 and PP-HC-17 are 0.0514, 0.0118 and 0.0037 $cm^3\ g^{-1}$, respectively, indicating

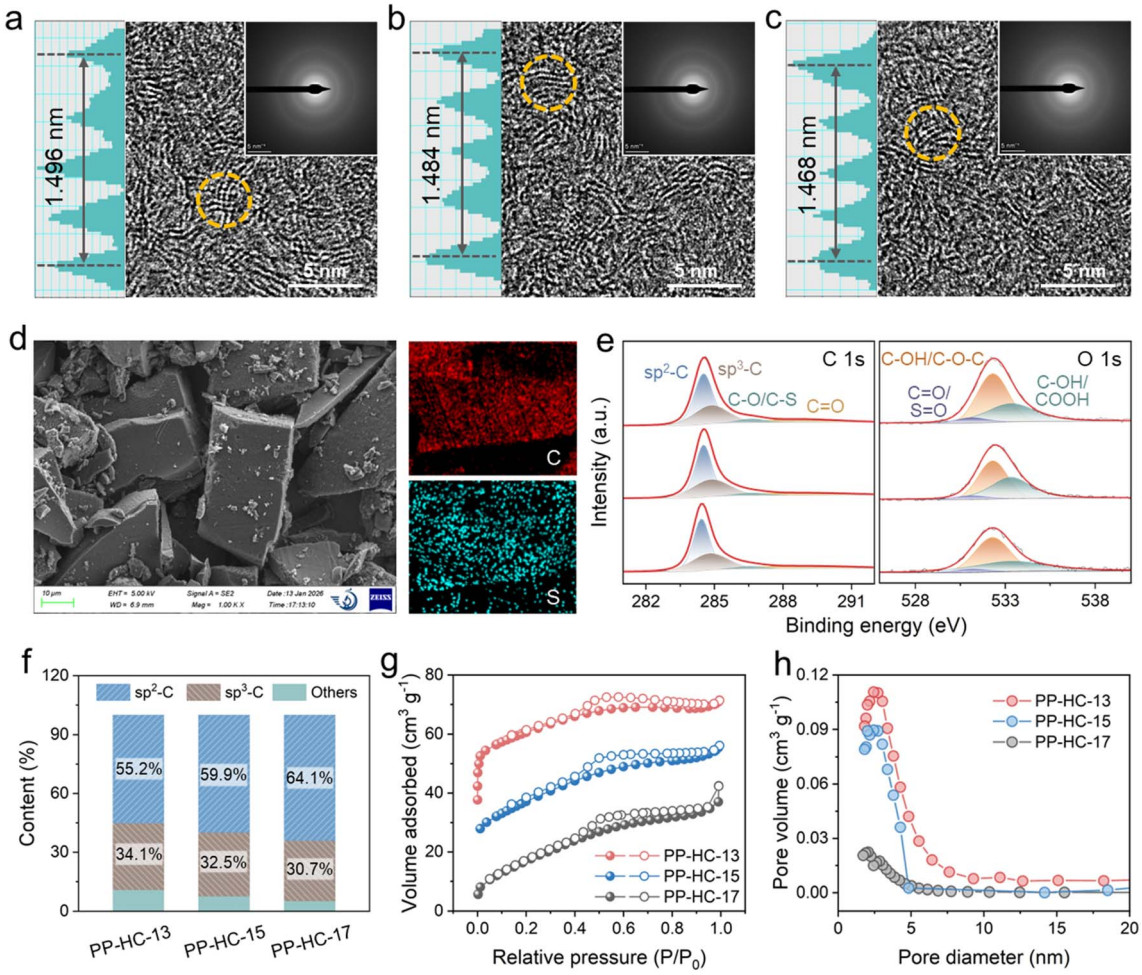

Fig. 3 HRTEM images of (a) PP-HC-13, (b) PP-HC-15, and (c) PP-HC-17 samples. (d) SEM image and EDS spectra of the PP-HC sample. High-resolution XPS spectra of (e) C 1s and O 1s. (f) The content of sp^2-C and sp^3-C in the three HC samples. (g) N_2 adsorption–desorption isotherms and (h) pore size distribution of PP-HC-13, PP-HC-15 and PP-HC-17 samples.

the decreased SSA and pore volume of PP-HC with the increase in temperature.

The structure evolution resulting from sulfonation-induced crosslinking has direct implications for sodium storage behavior. The electrochemical behaviors of the as-prepared PP-HC anodes were first evaluated by cyclic voltammetry (CV) measurements, as shown in Fig. 4a. The appearance of a pair of reversible redox peaks can be observed in the CV curves of the PP-HC anodes, which are related to the intercalation and deintercalation of Na^+ in the graphitic layers and nanopores.[29] The CV curves were well overlapped in the subsequent cycles, indicating the excellent reversibility and cyclic stability of the anodes. The electrochemical performance of the electrodes was further investigated by galvanostatic charging/discharging (GCD) measurements, as provided in Fig. 4b. Notably, the PP-HC-15 anode shows a higher initial coulombic efficiency (ICE) of 72.6% and reversible capacity of 293.3 mAh g^{-1}, compared to PP-HC-13 (68.5% and 207.0 mAh g^{-1}) and PP-HC-17 (68.8% and 227.9 mAh g^{-1}). The capacity loss during the initial cycles resulted mainly from interfacial side reactions and the formation of an SEI film. Additionally, the sloping region of the discharge profile is associated mainly with Na^+ adsorption at defect sites, edges, and near-surface regions, which correlates with the presence of structural disorder and accessible surface sites. In contrast, the low-potential plateau capacity is closely related to Na^+ insertion between turbostratic carbon layers and/or Na^+ filling within nanopores, both of which are facilitated by the enlarged interlayer spacing and confined pore structure. Therefore, by chemically regulating the carbonization pathway of recycled PP separators, sulfonation-induced crosslinking enables the construction of structure-tailored hard carbon with a balanced combination of adsorption- and insertion-dominated sodium storage, leading to enhanced Na^+ transport and storage kinetics. As illustrated in Fig. 4c, the plateau-contribution capacity was significantly enhanced along with the increase in carbonization temperature, which is generated by the decrease in defects and the increase in graphitization of the PP-HC as the temperature rises.

Fig. 4d shows the cyclic stability of the anodes at 0.2C, where the reversible capacity of the PP-HC-15 anode remained at 267.0

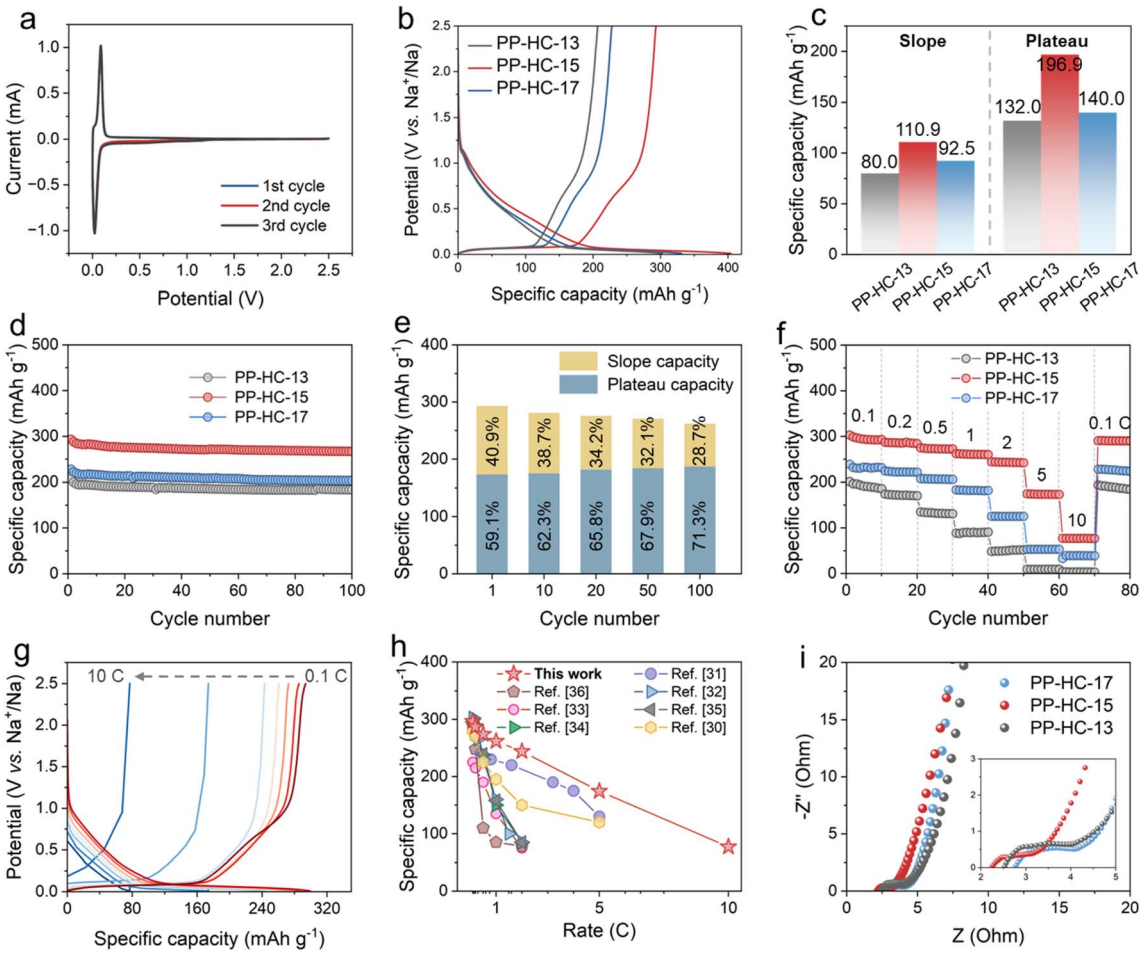

Fig. 4 (a) CV curves of PP-HC anode for the initial cycles with a scan rate of 0.1 mV s^{-1}. (b) Charge–discharge curves, and (c) capacity contribution of slope and plateau of PP-HC-13, PP-HC-15 and PP-HC-17 electrodes for the first cycle. (d) Cyclic performance and (e) capacity contribution of the three anodes at 0.2C. (f) Rate capability and (g) corresponding charge–discharge curves of the anodes at different current densities. (h) Comparison of the rate performance of PP-HC-15 with previously reported HC-based anodes.[30–36] (i) EIS spectra of PP-HC-13, PP-HC-15 and PP-HC-17 electrodes.

mAh g^{-1} after 100 cycles with a capacity retention of 91.0%, higher than those for PP-HC-13 and PP-HC-17 electrodes. Accordingly, the plateau- and slope-contribution capacities remain almost unchanged as the cycle progresses (Fig. 4e), indicating stable Na^+ ion adsorption and pore-filling behavior. Fig. 4f demonstrates the rate capability of the three electrodes. PP-HC-15 delivers capacities of 296.7, 287.1, 274.0, 261.7, 243.9, 174.4 and 77.1 mAh g^{-1} at current densities of 0.1, 0.2, 0.5, 1, 2, 5 and 10C. When the current density returned to 0.1C, the capacity recovered to 290.9 mAh g^{-1}. In contrast, the PP-HC-13 and PP-HC-17 electrodes show much lower capacities at the same current densities. Notably, the capacity of PP-HC-13 is almost not retained at 10C. Moreover, the distinct plateau and sloping regions in the voltage profiles were preserved even at a high current density of 10C (Fig. 4g), demonstrating superior Na^+ ion transport kinetics with a slight polarization effect in PP-

Table 1 Performance comparison of the HC in this work with the representative HCs for SIBs reported in recent years

Precursor	Capacity (mAh g^{-1})	ICE	Rate capability (mAh g^{-1})	Cyclic stability	Ref.
Resin-based polymers	257.7	75%	157 at 5 A g^{-1}	54% retention after 2000 cycles	40
Phenolic resin	293.5	68%	162.5 at 5 A g^{-1}	71% retention after 2000 cycles	41
Asphalt	313.8	86%	130 at 5C	90% retention after 200 cycles	31
Coal	308.4	82%	85 at 2C	85% retention after 800 cycles	32
Coal	253	73%	140 at 1 A g^{-1}	80% retention after 500 cycles	42
PP	296.7	69%	77.1 at 10C	89% retention after 1000 cycles	This work

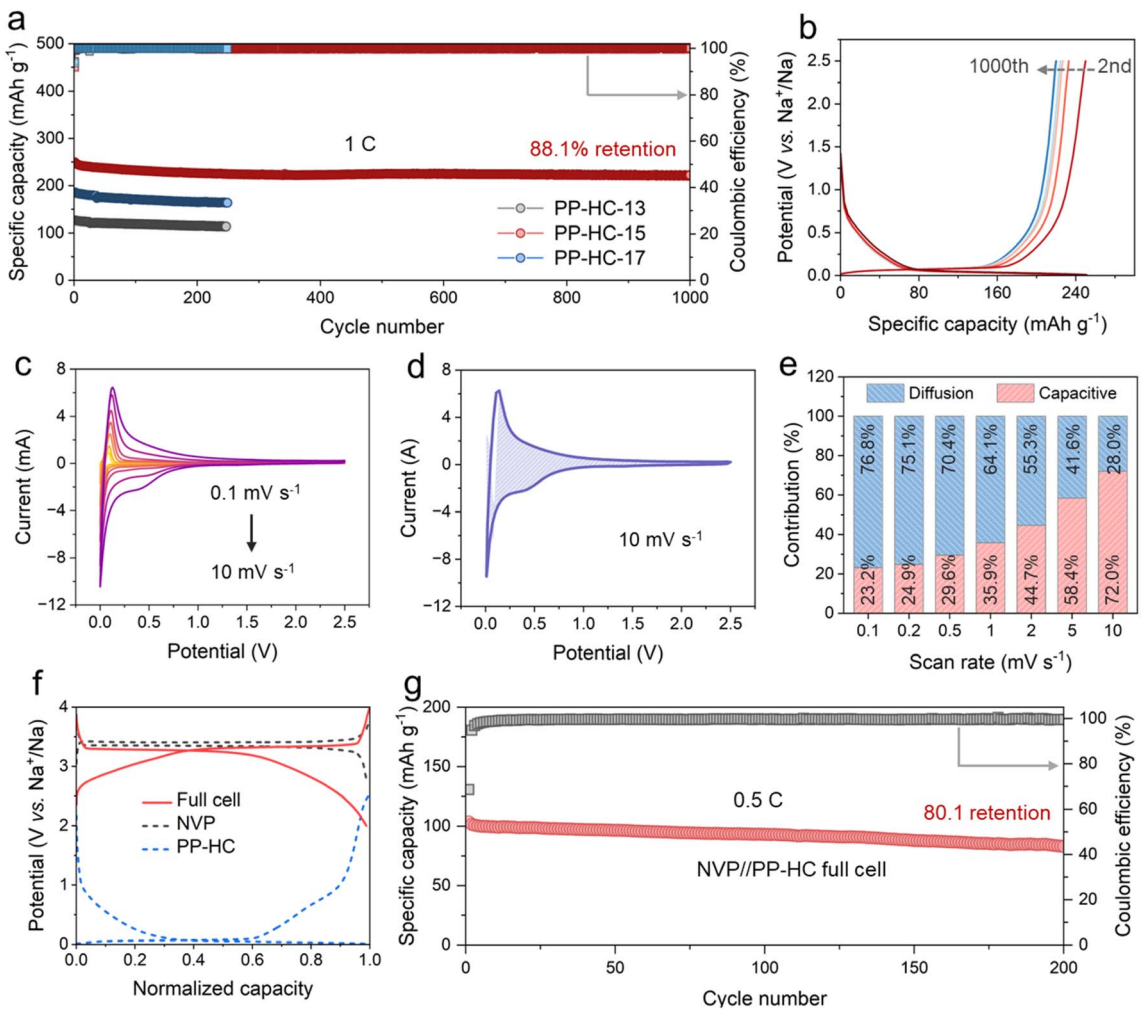

Fig. 5 (a) Long-term cyclic performance of PP-HC-13, PP-HC-15 and PP-HC-17 anodes. (b) Charge–discharge profiles of PP-HC-15 from the 2nd cycle to the 1000th cycle. (c) CV curves of the PP-HC-15 anode at various scan rates. (d) Charge storage contribution from capacitive storage at a scan rate of 10 mV s^{-1}. (e) Capacity contribution of a PP-HC-15 anode. (f) Charge–discharge curves of NVP|Na and PP-HC|Na half cells, with an NVP||PP-HC full cell. (g) Cyclic performance of NVP||PP-HC full cell.

HC-15 electrodes. This outstanding performance can be attributed to the suitable graphitic structure of PP-HC-15, which distinguishes it from numerous previously reported state-of-the-art HC-based anodes,[30–36] as illustrated in Fig. 4h and Table 1. Electrochemical impedance spectroscopy (EIS) spectra of the as-prepared anodes are presented in Fig. 4i, demonstrating the lower charge transfer impedance and faster Na^+ diffusion of the PP-HC-15 electrode. In consideration of the excellent rate capability, the anodes were further cycled at 1C to investigate their long-term cyclic performance (Fig. 5a). After 1000 cycles, the capacity of PP-HC-15 remained at 222.7 mAh g^{-1} with a capacity retention of 89.1%, much higher than those of PP-HC-13 (113.7 mAh g^{-1} after 247 cycles) or PP-HC-17 (163.7 mAh g^{-1} after 249 cycles) electrodes. Fig. 5b presents the charge–discharge profiles of PP-HC-15 recorded from the 2nd to the 1000th cycles at 1C, which show the remarkable consistency and exceptional reversibility of sodium storage.

The Na^+ storage behavior and kinetics of PP-HC-15 in an ester-based electrolyte were further investigated. Fig. 5c provides the CV curves of PP-HC-15 at different scan rates from 0.1 to 10 mV s^{-1}. As is known from the power-law correlation, the relationship of current (i) and scan rate (v) can be described by the formula $i = a \cdot v^b$, where a and b are constants.[37–39] The values of $b = 1$ and 0.5 reveal the capacitive effects of pseudo-capacitance and non-faradaic reaction, the sum of which is the total current, as described by $i(V) = k_1 v + k_2 v^{1/2}$. Here, $k_1 v$ and $k_2 v^{1/2}$ represent the capacitive behavior and diffusion process, respectively. According to the values of k_1 and k_2, the capacity contribution of PP-HC-15 at different scan rates can be estimated (Fig. 5d). As shown in Fig. 5e, the ratio of pseudo-capacity was enhanced from 23.2% to 72.0% with the increase in scan rate, leading to the high-rate capability of the PP-HC-15 electrode.

In order to verify the practicality of the as-prepared anode, full cells were designed by using $Na_3V_2(PO_4)_3$ (NVP) as a cathode and PP-HC-15 as an anode. The corresponding charge–discharge curves of NVP|Na and PP-HC-15|Na half cells and an NVP||PP-HC-15 full cell are provided in Fig. 5f. As can be seen, the full cell shows similar charge–discharge curves, which is attributed mainly to the phase transition on the cathode side and the adsorption-filling kinetics on the anode side. For long-term cycling at 0.5C in Fig. 5g, the capacity shows a slight decay after 200 cycles with a capacity of 83.0 mAh g^{-1} and 80.1% retention, corresponding to a very low capacity loss of 0.0995% per cycle. This result indicates the excellent cyclic performance of the full cell, demonstrating the attractive commercialization prospects of recycled polypropylene separator-derived hard carbon.

3. Conclusions

In summary, a sulfonation-induced crosslinking strategy was developed to regulate the carbonization behavior of recycled PP separators and enable their conversion into structure-tailored HC anodes for SIBs. The introduction of sulfonic functionalities not only modifies the chemical environment of PP chains but also induces intermolecular crosslinking, which effectively suppresses severe chain scission and volatilization during thermal treatment. As a result, the carbonization pathway of PP is transformed from a volatilization-dominated decomposition to a solid-state carbonization process, leading to an increased carbon yield and the formation of a continuous carbon framework. Systematic structural characterization reveals that the sulfonation-induced crosslinking plays a decisive role in the evolution of a hard carbon microstructure. The optimized carbonization process promotes the formation of turbostratic carbon domains with enlarged interlayer spacing, moderate structural disorder, and a hierarchical pore structure, while suppressing long-range graphitization. When evaluated as anodes for sodium-ion batteries, the PP-derived HC delivers a high reversible capacity of 293.0 mAh g^{-1} at 0.2C and 77.1 mAh g^{-1} even at a high current density of 10C. For long-term cyclic performance, the capacity remained at 222.7 mAh g^{-1} after 1000 cycles at 1C with a capacity retention of 89.1%. When paired with an $Na_3V_2(PO_4)_3$ cathode, the full cell shows a capacity of 83 mAh g^{-1} after 200 cycles with 80.1% retention. This work demonstrates a feasible and scalable approach for the high-value recycling of spent lithium-ion battery separators. By chemically regulating the carbonization pathway of a typical polyolefin waste, this strategy bridges sustainable materials recycling with structure-oriented hard carbon design. The insights gained from this study provide guidance for the rational construction of hard carbon anodes and may be extended to other polymer-derived carbon systems for sodium-ion and related energy storage technologies.

4. Experimental section

4.1 Materials preparation

All chemical reagents and solvents are commercially available without further purification. Typically, the recycled PP separators were washed with ultrapure water and ethyl alcohol several times. Then, 1.5 g of PP separators were cut into pieces and soaked in 100 mL of sulfuric acid (98%) at 120 °C for 6 h, after which the sulfonated PP separators were washed with ultrapure water and ethyl alcohol to remove the remaining sulfuric acid. The resultant samples were dried in a vacuum oven at 80 °C for 12 h and designated as sulfonated PP. Afterwards, the obtained samples were transferred into a tubular furnace held at 700 °C for 1 h and then heated for 30 min at 1300, 1500 or 1700 °C at a heating rate of 5 °C min^{-1}. The obtained samples were labelled PP-HC-13, PP-HC-15 and PP-HC-17, respectively. Finally, the products were ground to a fine powder by ball milling for 4 h.

4.2 Materials characterization

Differential scanning calorimetry (DSC, Mettler Toledo DSC822E) and thermogravimetric analysis (TGA, Mettler Toledo) were employed to analyze the thermal behaviors of recycled and sulfonated PP separators. A Bruker D8 Advance X-ray diffractometer using Cu Kα radiation (λ = 1.5418 Å) was utilized to detect the crystal structure of the materials. Raman spectroscopy was undertaken with a Horiba LabRAM HR

Evolution Raman microscope using 514 and 532 nm lasers. The surface chemical states and functional groups were studied by X-ray photoelectron spectroscopy (XPS) with a Thermo Fisher ESCALAB Xi+ system. A Micromeritics ASAP2460 instrument based on the Brunauer–Emmett–Teller (BET) method was used to investigate the pore structure of the samples.

4.3 Electrochemical measurements

To prepare the working electrode, the as-prepared PP-HC, Super P and polyvinylidene fluoride were mixed in a ratio of 8 : 1 : 1 in *N*-methylpyrrolidone to form a homogeneous slurry, which was then coated onto Cu foil and dried under vacuum conditions at 80 °C for 12 h. The typical mass loading of the active material was 1.2–1.7 mg cm^{-2}. The coin cells (CR2016) were assembled inside an argon-filled glovebox (H_2O, O_2 < 0.01 ppm) for electrochemical testing. For half-cells, sodium metal, glass fiber and 1 M $NaPF_6$ in DME were used as counter electrode, separator and electrolyte, respectively. Galvanostatic charge–discharge tests were conducted on a LANHE Battery Test System (CT3002A, Wuhan) at 30 °C. CV and EIS testing were performed on a Chenhua electrochemical workstation (CHI660A, Shanghai). The full cell was assembled with $Na_3V_2(PO_4)_3$, PP-HC, and 1 M $NaPF_6$ in DME as cathode, anode and electrolyte, respectively. The galvanostatic charge–discharge tests were carried out in the voltage range 2.0–4.0 V.

Author contributions

Mingyue Wang: conceptualization, writing – original draft, supervision, writing – review & editing. Yue Wang & Na Li: formal analysis. Qing Zhong & Min Zhu: investigation. Dongyang Zhang & Shujiang Ding: funding acquisition, supervision.

Conflicts of interest

There are no conflicts of interest to declare.

Data availability

The data that support the findings of this study are available from the corresponding author upon reasonable request.

Acknowledgements

This work is financially supported by the National Natural Science Foundation of China (52202297), Xi'an Association for Science Technology Young Talent Support Program Project (0959202513149) and Innovation Capability Support Plan of Shaanxi (no. 2022TD-27). We deeply acknowledge Mr Zijun Ren at Instrumental Analysis Center of Xi'an Jiaotong University for the assistance with SEM. The authors would like to thank Scientific Compass (https://www.shiyanjia.com/) for the assistance of Raman testing.

References

1 J. Wu, Z. Song, Q. Huang, K. Zhu, D. Lin, X. Chen, X. Li, X. Chen, X. Li, L. Ma and Y. Chen, Electrolyte Engineering for Room-Temperature Sodium–Sulfur Batteries: Challenges, Strategies, and Future Perspectives, *Adv. Mater.*, 2026, **38**, e14290.
2 L. Miao, Z. Guo and L. Jiao, Insights into the design of mildly acidic aqueous electrolytes for improved stability of Zn anode performance in zinc-ion batteries, *Energy Mater.*, 2023, **3**, 300014.
3 N. LeGe, Y.-H. Zhang, W.-H. Lai, X.-X. He, Y.-X. Wang, L.-f. Zhao, M. Liu, X. Wu and S.-L. Chou, Potassium escaping balances the degree of graphitization and pore channel structure in hard carbon to boost plateau sodium storage capacity, *Chem. Sci.*, 2025, **16**, 1179–1188.
4 T. Wei, X.-L. Xian, S.-X. Dou, W. Chen and S.-L. Chou, Comprehensive analysis and mitigation strategies for safety issues of sodium-ion batteries, *Rare Met.*, 2024, **43**, 1343–1349.
5 X. Cai, Y. Yue, Z. Yi, J. Liu, Y. Sheng and Y. Lu, Challenges and industrial perspectives on the development of sodium ion batteries, *Nano Energy*, 2024, **129**, 110052.
6 Y. Sun, R. Hou, S. Xu, H. Zhou and S. Guo, Molecular Engineering Enabling High Initial Coulombic Efficiency and Rubost Solid Electrolyte Interphase for Hard Carbon in Sodium-Ion Batteries, *Angew. Chem., Int. Ed.*, 2024, **63**, e202318960.
7 C. Wu, Y. Yang, Y. Zhang, H. Xu, X. He, X. Wu and S. Chou, Hard carbon for sodium-ion batteries: progress, strategies and future perspective, *Chem. Sci.*, 2024, **15**, 6244–6268.
8 C. Wu, Y. Yang, Y. Zhang, H. Xu, W. Huang, X. He, Q. Chen, H. Dong, L. Li, X. Wu and S. Chou, Industrial-Scale Hard Carbon Designed to Regulate Electrochemical Polarization for Fast Sodium Storage, *Angew. Chem., Int. Ed.*, 2024, **63**, e202406889.
9 Y. Zeng, J. Yang, H. Yang, Y. Yang and J. Zhao, Bridging Microstructure and Sodium-Ion Storage Mechanism in Hard Carbon for Sodium Ion Batteries, *ACS Energy Lett.*, 2024, **9**, 1184–1191.
10 Z.-G. Liu, J. Zhao, H. Yao, X.-X. He, H. Zhang, Y. Qiao, X.-Q. Wu, L. Li and S.-L. Chou, P-doped spherical hard carbon with high initial coulombic efficiency and enhanced capacity for sodium ion batteries, *Chem. Sci.*, 2024, **15**, 8478–8487.
11 C. Wu, Y. Yang, Y. Li, X. He, Y. Zhang, W. Huang, Q. Chen, X. Liu, S. Chen, Q. Gu, L. Li, S. C. Smith, X. Tan, Y. Yu, X. Wu and S. Chou, Unraveling the structure–performance relationship in hard carbon for sodium-ion battery by coupling key structural parameters, *Energy Environ. Sci.*, 2025, **18**, 6019–6031.
12 M.-Y. Su, K.-Y. Zhang, E. H. Ang, X.-L. Zhang, Y.-N. Liu, J.-L. Yang, Z.-Y. Gu, F. A. Butt and X.-L. Wu, Structural regulation of coal-derived hard carbon anode for sodium-ion batteries via pre-oxidation, *Rare Met.*, 2024, **43**, 2585–2596.

13 S. Pothaya, C. Poochai, N. Tammanoon, Y. Chuminjak, T. Kongthong, T. Lomas, C. Sriprachuabwong and A. Tuantranont, Bamboo-derived hard carbon/carbon nanotube composites as anode material for long-life sodium-ion batteries with high charge/discharge capacities, *Rare Met.*, 2024, **43**, 124–137.
14 W.-Y. Qian, X.-Y. Zhou, X.-Y. Liu, M.-Y. Su, K.-Y. Zhang and X.-L. Wu, Breakage of the dense structure of coal precursors increases the plateau capacity of hard carbon for sodium storage, *Chem. Sci.*, 2025, **16**, 104–112.
15 S. Wang, J. Dou, R. Holze, T. Zhang, L. Ye, L. Duan, J. Xue, S. Li and X. Chen, Recent Progress in Polymer Waste-Derived Porous Carbon for Supercapacitors, *Chemelectrochem*, 2023, **10**, e202300223.
16 J. Lin, Q. Zhou, Z. Liao, Y. Chen, Y. Liu, Q. Liu and X. Xiong, Steric Hindrance Engineering to Modulate the Closed Pores Formation of Polymer-Derived Hard Carbon for High-Performance Sodium-Ion Batteries, *Angew. Chem., Int. Ed.*, 2024, **63**, e202409906.
17 F. Wen, X. He, S. Sun, W. Jian, R. Dai, Q. Meng, K. Lu, X. Qiu and W. Zhang, Production of polypropylene-derived novel porous carbon nanosheets through aromatization stabilization toward supercapacitor applications, *Chem. Eng. Sci.*, 2023, **270**, 118559.
18 L. Qiu, H. Liu, M. Jiang, H. Zhang, C. Zeng, Q. Guo and S. Chen, Sustainable upcycling of polypropylene-based masks into high-performance carbon materials for supercapacitors via molten salt carbonization and air activation, *J. Energy Storage*, 2025, **119**, 116249.
19 Y. Yang, S. Sreekumar, R. V. Chimenti, M. Veksler, K. Song, S. Zhang, D. Rodas, V. Christianson and D. M. O'Carroll, Polypropylene-Derived Luminescent Carbon Dots, *ACS Mater. Lett.*, 2024, **6**, 1968–1976.
20 J. Ni, K. Huang, Q. Qin, Y. Wang, X. Yang, P. Liu, Y. Yang, F. Yu and J. Ma, Polypropylene-derived iron sulfide/carbon nanoflower for high performance electrochemical dechlorination, *J. Colloid Interface Sci.*, 2026, **705**, 139491.
21 D. Choi, D. Jang, H.-I. Joh, E. Reichmanis and S. Lee, High Performance Graphitic Carbon from Waste Polyethylene: Thermal Oxidation as a Stabilization Pathway Revisited, *Chem. Mater.*, 2017, **29**, 9518–9527.
22 H. U. Modekwe, M. A. Mamo, K. Moothi and M. O. Daramola, Effect of Different Catalyst Supports on the Quality, Yield and Morphology of Carbon Nanotubes Produced from Waste Polypropylene Plastics, *Catalysts*, 2021, **11**, 692.
23 G. Lee, M. Eui Lee, S.-S. Kim, H.-I. Joh and S. Lee, Efficient upcycling of polypropylene-based waste disposable masks into hard carbons for anodes in sodium ion batteries, *J. Ind. Eng. Chem.*, 2022, **105**, 268–277.
24 D. Choi, S. H. Yoo and S. Lee, Safer and more effective route for polyethylene-derived carbon fiber fabrication using electron beam irradiation, *Carbon*, 2019, **146**, 9–16.
25 F. J. Lanyi, N. Wenzke, J. Kaschta and D. W. Schubert, On the Determination of the Enthalpy of Fusion of α-Crystalline Isotactic Polypropylene Using Differential Scanning Calorimetry, X-Ray Diffraction, and Fourier-Transform Infrared Spectroscopy: An Old Story Revisited, *Adv. Eng. Mater.*, 2020, **22**, 1900796.
26 M. Wang, H. Zhao, Y. Wang, N. Li, X. Liu, D. Zhang, K. Xi and S. Ding, Melt-carbonization of liquid metal organic frameworks reconfigured hard carbon surface with boosted sodium storage, *Sci. China Chem.*, 2025, **69**, 1467–1474.
27 J. Choi, S.-S. Kim, Y.-S. Chung and S. Lee, Evolution of structural inhomogeneity in polyacrylonitrile fibers by oxidative stabilization, *Carbon*, 2020, **165**, 225–237.
28 H. Xie, Z. Wu, Z. Wang, N. Qin, Y. Li, Y. Cao and Z. Lu, Solid electrolyte interface stabilization via surface oxygen species functionalization in hard carbon for superior performance sodium-ion batteries, *J. Mater. Chem. A*, 2020, **8**, 3606–3612.
29 M. Liu, F. Wu, Y. Gong, Y. Li, Y. Li, X. Feng, Q. Li, C. Wu and Y. Bai, Interfacial-Catalysis-Enabled Layered and Inorganic-Rich SEI on Hard Carbon Anodes in Ester Electrolytes for Sodium-Ion Batteries, *Adv. Mater.*, 2023, **35**, 2300002.
30 H. Wang, S. Liu, C. Lei, H. Qiu, W. Jiang, X. Sun, Y. Zhang and W. He, P-doped hard carbon material for anode of sodium ion battery was prepared by using polyphosphoric acid modified petroleum asphalt as precursor, *Electrochim. Acta*, 2024, **477**, 143812.
31 L. Wang, Z. Xu, P. Lin, Y. Zhong, X. Wang, Y. Yuan and J. Tu, Oxygen-Crosslinker Effect on the Electrochemical Characteristics of Asphalt-Based Hard Carbon Anodes for Sodium-Ion Batteries, *Adv. Energy Mater.*, 2025, **15**, 2403084.
32 K. Wang, F. Sun, H. Wang, D. Wu, Y. Chao, J. Gao and G. Zhao, Altering Thermal Transformation Pathway to Create Closed Pores in Coal-Derived Hard Carbon and Boosting of Na+ Plateau Storage for High-Performance Sodium-Ion Battery and Sodium-Ion Capacitor, *Adv. Funct. Mater.*, 2022, **32**, 2203725.
33 Y. Li, Y.-S. Hu, X. Qi, X. Rong, H. Li, X. Huang and L. Chen, Advanced sodium-ion batteries using superior low cost pyrolyzed anthracite anode: towards practical applications, *Energy Storage Mater.*, 2016, **5**, 191–197.
34 H. Zhou, N. Sun, J. Yu, R. A. Soomro, S. Zhang and B. Xu, Microstructure regulation of resin-based hard carbons via esterification cross-linking for high-performance sodium-ion batteries, *Inorg. Chem. Front.*, 2023, **10**, 2404–2413.
35 H. Zhang, H. Ming, W. Zhang, G. Cao and Y. Yang, Coupled Carbonization Strategy toward Advanced Hard Carbon for High-Energy Sodium-Ion Battery, *ACS Appl. Mater. Interfaces*, 2017, **9**, 23766–23774.
36 J. Peng, H. Tan, Y. Tang, J. Yang, P. Liu, J. Liu, K. Zhou, P. Zeng, L. He and X. Wang, The induced formation and regulation of closed-pore structure for biomass hard carbon as anode in sodium-ion batteries, *J. Energy Storage*, 2024, **101**, 113864.
37 M. Wang, H. Zhang, C. Chen, H. Zhao, L. Li, D. Lu, J. Wang, Y. Huang and S. Ding, Zeolitic imidazolate framework-derived ZnO polyhedrons wrapped by Co nanoparticle embedded in N-doped carbon for high-performance lithium and potassium storage, *J. Alloys Compd.*, 2023, **948**, 169677.
38 X. Lu, J. Zhou, L. Huang, H. Peng, J. Xu, G. Liu, C. Shi and Z. Sun, Low-Temperature Carbonized N/O/S-Tri-Doped

Hard Carbon for Fast and Stable K-Ions Storage, *Adv. Energy Mater.*, 2024, **14**, 2303081.

39 X. Lu, J. Zhou, X. Li, H. Peng, C. Shi, F. Liu, L. Huang and Z. Sun, In Situ Composite Strategy of O/F-Dual-Doped Soft–Hard Carbon Anode Promotes Ultrafast and Highly Durable Potassium Storage Performance, *ACS Appl. Mater. Interfaces*, 2025, **17**, 29708–29719.

40 S. Wu, H. Peng, J. Xu, L. Huang, Y. Liu, X. Xu, Y. Wu and Z. Sun, Nitrogen/phosphorus co-doped ultramicropores hard carbon spheres for rapid sodium storage, *Carbon*, 2024, **218**, 118756.

41 S. Wu, H. Peng, L. Huang, Y. Liu, Y. Wu, L. Liu, W. Ai and Z. Sun, P-doped hard carbon microspheres for sodium-ion battery anodes with superior rate and cyclic performance, *Inorg. Chem. Front.*, 2023, **10**, 5908–5916.

42 R. Li, B. Yang, A. Hu, B. Zhou, M. Liu, L. Yang, Z. Yan, Y. Fan, Y. Pan, J. Chen, T. Li, K. Li, J. Liu and J. Long, Heteroatom screening and microcrystal regulation of coal-derived hard carbon promises high-performance sodium-ion batteries, *Carbon*, 2023, **215**, 118489.